RSC Advances

PAPER

View Article Online
View Journal | View Issue

Cite this: *RSC Adv.*, 2026, **16**, 29661

Elucidating the role of PdAgFe charge transfer in ternary aerogels for boosting electro-oxidative degradation of recalcitrant di-butyl phthalate

Sammia Khurshid,[a] Muzammil Anjum, *[a] Rab Nawaz,[b] Sahar Saleem,[c] Marlia Mohd Hanafiah,[bd] Azeem Khalid[a] and Muhammad Umair[e]

Received 11th January 2026
Accepted 10th April 2026

DOI: 10.1039/d6ra00270f

rsc.li/rsc-advances

In this work, Pd-based aerogels were modified with transition metals (Ag, Fe) for the degradation and electrochemical oxidation of di-butyl phthalate (DBP) in water. The newly synthesized PdAgFe aerogel showed a uniform dispersion with a practical size of 4–9 nm, and achieved a dense interconnected network revealed by transmission electron microscopy. The PdAgFe-assisted electrochemical oxidation of DBP achieved 97% removal at a pollutant concentration of 90 mg L^{-1}, surpassing that of pollutant concentrations of 90 mg L^{-1}, surpassing that of binary aerogels, *i.e.*, PdFe (86.3%) and PdAg (70.6%). The oxygen evolution potential of PdAgFe increased progressively from 1.61 to 1.97 V with maximum applied DBP concentration. This reflects the enhanced catalytic selectivity and activity of PdAgFe at the optimum operating scan rate (5 mV s^{-1}) in 1 M KOH over 8 h of process duration. Kinetic modeling confirmed that DBP degradation followed a pseudo-first-order rate law, with PdAgFe showing the highest apparent rate constant (k = 0.36 h^{-1}, R^2 = 0.99) at 90 mg L^{-1}. This enhanced electrochemical potential of PdAgFe is associated with its strong structural and electronic characteristics. For instance, XPS analysis revealed Fe^{3+} oxidation states and a positive shift in Pd 3d binding energy to 334.32 eV, indicative of strong electronic coupling within the trimetallic framework. Our findings provide valuable insights into cost-effective Pd-engineered aerogels with transition metals to enhance the catalytic removal of DBP.

1. Introduction

Rapid industrial development has led to the release of toxic pollutants into water bodies, which have negative impacts on both the environment and human health. Phthalates are plasticizers widely used in the plastics industry. Among phthalates, dibutyl phthalate (DBP) is one of the most widely used, especially in industrial solvents, adhesives, waxes, inks, medicines, and cosmetics. DBP is considered an endocrine-disrupting chemical (EDC) due to its biological toxicity and is classified as a primary pollutant.[1]

It has been found that DBP can affect the human body, damaging the endocrine and immune systems and causing various neurological effects, even at low concentrations. Due to the weak covalent interaction between DBP and conventional plastics, it is quickly released from the plastic matrix into the environment. This results in bioaccumulation in aquatic organisms, including those found in marine and freshwater environments.[2] In Pakistan, DBP has been detected in the Kabul and Swat rivers; however, it has not been detected in municipal and industrial wastewater.[3]

Currently, the different treatment technologies for phthalates include adsorption,[4] advanced oxidation,[5] and biodegradation,[6] *etc.* Adsorption and photo-oxidation are costly processes and generate secondary pollutants, whereas biodegradation can effectively remove phthalates from water; however, the degradation rate is very slow and requires specific microbes.

Electrochemical oxidation is an advanced wastewater treatment technology with significant potential for practical application due to its high removal efficiency, operational flexibility, environmental sustainability, and precise control of reaction conditions.[7] Electrocatalysis is considered a viable and efficient treatment method due to its cost-effectiveness, strong capability for DBP degradation, and the simultaneous production of hydrogen at the cathode, which adds additional economic and environmental value.[8] A brief degradation pathway for DBP is illustrated below.[9]

At anode DBP oxidation:

[a]*Department of Environmental Sciences, PMAS Arid Agriculture University, 46300-Rawalpindi, Pakistan. E-mail: muzammilanjum@uaar.edu.pk; muzammilanjum@gmail.com; Tel: +92 51 9292 135*

[b]*Research Center for Industrial Nuclear Energy (IRC-INE), King Fahad University of Petroleum and Minerals (KFUPM), Dhahran 31261, Saudi Arabia*

[c]*Department of Sciences, School of Interdisciplinary Engineering and Sciences, National University of Sciences and Technology, Islamabad 44000, Pakistan*

[d]*Department of Earth Sciences and Environment, Faculty of Science and Technology, Universiti Kebangsaan Malaysia (UKM), 43600-Bangi, Selangor, Malaysia*

[e]*Faculty of Agricultural Engineering & Technology, PMAS-Arid Agriculture University, Rawalpindi 46000, Pakistan*

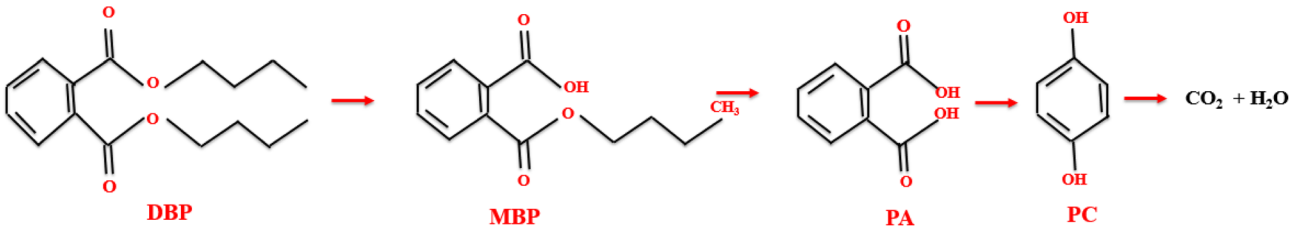

Although traditional catalysts such as Pt, Pd, and Rh exhibit good activity, they have limited industrial use on a large scale due to their high cost and scarcity. The research conducted in the last decade showed that transition metal compounds like alloys,[10] oxides,[11] nitrides,[12] selenides,[13] sulfides,[14] phosphides,[15] borides,[16] and carbides,[17] have been studied intensely. Among various porous materials, aerogels exhibit efficient physical properties, such as ultralow density (approaching 1.2×10^{-4} g cm^{-3}), high continuous porosity, and large surface areas of up to 1000 m^2 g^{-1}, giving them great significance in catalysis and other applications like energy storage, piezoelectric, thermoresistors, and sensors.[18] Different types of aerogels have been utilized for the degradation of different organic pollutants and hydrogen production, such as nickel,[19] cobalt,[20] iron,[21] and palladium.[22]

It was found that the Ce-doped Ti/PbO_2 electrode achieved removal efficiencies of 98.2% for DBP, 95.8% for DMP, and 81.1% for DEP (5 mg L^{-1} each) after 10 h at 25 mA cm^{-2} and pH 7. The degradation followed pseudo-first order kinetics with rate constants of 0.42 h^{-1} (DBP), 0.40 h^{-1} (DEP), and 0.29 h^{-1} (DMP). The electrode also demonstrated good stability and reusability.[23] In another study, the electrocatalytic degradation of dibutyl phthalate (DBP) was carried out using an IrO_2–Ta_2O_5/Ti anode with a graphite cathode. At 10 V cm^{-1} for 60 min, the process achieved 90% DBP and 56% TOC removal. It was more energy-efficient than photocatalysis, consuming nearly half the energy. Hydroxyl radicals ($^{\bullet}$OH) were the main active species responsible for DBP breakdown. The electrode demonstrated stability and reusability, maintaining 90% efficiency after three cycles. Similarly, photocatalysis combined with electrocatalytic oxidation (PC + EC) was applied to the removal of dibutyl phthalate (DBP). The V_2O_5 and a C/Ti anode were used for the degradation of DBP under optimized conditions, achieved 99.5% DBP degradation, 97% COD and 87.7% reduction in TOC. The hybrid PC + EC system showed 40% higher TOC removal than EC alone. Reusability tests indicated V_2O_5 performance declined, while the anode remained stable. Overall, PC + EC proved highly effective for treating poorly soluble pollutants like phthalates.[24]

In another study, a PTFE-doped PbO_2 anode on TiO_2 nanotubes was applied for DBP degradation. The electrode showed improved hydrophobicity, higher oxygen evolution potential, and greater ·OH generation. DBP removal efficiency followed the order: Ti/TiO_2NTs/PbO_2-PTFE > Ti/TiO_2NTs/PbO_2 > Ti/PbO_2. Kinetic studies revealed pseudo-first-order behavior with rate constants of 0.1326, 0.1266, and 0.1041 h^{-1}. The PTFE electrode achieved the lowest energy consumption (6.1 kWh g^{-1}) compared to 6.7 and 7.4 kWh g^{-1} for the others.[25]

While palladium-based aerogels integrated with transition metals have been extensively explored for various electrocatalytic processes, their application to phthalates degradation is still limited. The Pd : Ag : Fe (1 : 2 : 2) ratio was selected to maximize synergistic interactions while minimizing Pd usage. Pd was kept at a lower proportion due to its high intrinsic activity and cost, while higher Ag content enhances electronic modulation and conductivity, improving Pd dispersion and catalytic efficiency.[26] Ag-rich Pd–Ag systems (*e.g.*, Pd_1Ag_2) have been reported to show superior performance due to charge redistribution and weakened Pd–Pd interactions. Fe was incorporated at an equivalent level to Ag to introduce redox-active sites (Fe^{2+}/Fe^{3+}) and improve adsorption and structural stability, as widely reported for Fe-containing multi-metal systems in water treatment. Together, the 1 : 2 : 2 composition provides a balanced system, that combines Pd activity, Ag-induced electronic enhancement, and Fe-based redox/adsorptive functionality.[27,28]

The superior catalytic performance of the trimetallic PdAgFe aerogel compared to its bimetallic counterparts (PdAg and PdFe) can be theoretically justified based on electronic modulation and synergistic effects introduced by the third metal. Incorporation of Fe into Pd-based systems can shift the d-band center of Pd, alter charge distribution, and optimize the adsorption strength of reaction intermediates, thereby improving catalytic kinetics.[29] In alkaline electrooxidation systems, Fe species are also known to facilitate OH^- activation, promoting a bifunctional mechanism in which Pd provides active sites for organic adsorption while Fe enhances surface oxyhydroxide formation, accelerating oxidation reactions.[30] The addition of Ag further improves electrical conductivity and structural stability, contributing to enhanced electron transfer dynamics.[31] Moreover, the three-dimensional porous aerogel structure provides a continuous conductive network with high surface area and interconnected macropores/mesopores, which significantly enhance the exposure and mass transport of DBP molecules and electrolyte ions.[32] Such hierarchical porous frameworks minimize diffusion limitations and facilitate rapid charge transfer, ultimately leading to improved electrochemical degradation efficiency. Therefore, the combined electronic

synergy of the trimetallic system and the structural advantages of the aerogel architecture account for the enhanced catalytic activity observed for PdAgFe.

Moreover, the synthesis and utilization of a trimetallic PdAgFe aerogel for the electrochemical oxidation of phthalate pollutants have not yet been reported in the literature. Therefore, this study introduces a novel PdAgFe aerogel with enhanced electrocatalytic activity, addressing a critical research gap and offering a promising strategy for phthalate remediation. Hence, in the current study, palladium-based aerogels along with transition-metals such as PdAgFe, PdAg, and PdFe were synthesized, and the performance of the catalysts was investigated for electrocatalytic degradation of DBP. Factors influencing the performance were studied, including different scan rates and different DBP concentrations.

2. Materials and methods

2.1 Reagents

Silver nitrate $AgNO_3$ (Sigma-Aldrich 99.9%), palladium chloride $PdCl_2$ (Sigma-Aldrich 99.9%), ferric chloride hexahydrate $FeCl_3 \cdot 6H_2O$ (Sigma-Aldrich 99.9%), sodium hydroxide NaOH (Sigma-Aldrich 99.9%), sodium borohydride $NaBH_4$ (Sigma-Aldrich 96%), Acetone (Sigma-Aldrich $\geq$ 99.8%) were received from Merck. Sulphuric acid (Analar, 98.07%) and dibutyl phthalate (Daejung, 99%) were used in deionized water (MilliQ, 18.2 MΩ) throughout all experiments for preparing aqueous solutions.

2.2 Synthesis of aerogel

Palladium-based aerogels, PdAgFe, PdAg, and PdFe were prepared by using the co-precipitation method with little modification from previous literature. The precursor solutions were obtained by dissolving the metal precursor in deionized water. The metal content was 20 mM Ag, 20 mM Fe, and 10 mM $PdCl_2$ in 100 mL of deionized water. Initially, isolated solutions were prepared for each metal, then mixed with constant stirring. After 10 min of vigorous stirring, 11 mL of a sodium citrate solution (1 wt%) was added for the fine particles. Surface oxidation of the metallic components in the PdAgFe aerogel was minimized by employing sodium borohydride ($NaBH_4$) as a strong reducing agent and processing under cryogenic conditions using liquid nitrogen. $NaBH_4$ enabled rapid reduction of Pd^{2+}, Ag^{+}, and Fe^{3+}/Fe^{2+} to their zero-valent states, limiting exposure of intermediate species to dissolved oxygen. The use of liquid nitrogen significantly suppressed oxidation kinetics and reduced dissolved oxygen, thereby stabilizing freshly formed metallic surfaces during gelation. This combined reductive and cryogenic approach is well established for preserving metallic states in multimetallic nanostructures and aerogels.

One min later, the freshly prepared, ice-cold reducing agent solution containing 0.11 mmol of $NaBH_4$ and 0.5 M NaOH was added as shown in Fig. 1. The solution was kept stirring for another 5 to 10 min. After three days of settling, the hydrogels were prepared at the bottom of a glass vial. The as-prepared hydrogels were washed several times with deionized water and ethanol. Finally, the hydrogels were freeze-dried with liquid nitrogen, which led to the formation of aerogel. After that, the aerogel has been tested for its electrocatalytic potential in the electrolysis process.[33]

2.3 Wastewater sampling and characterization

Waste water samples have been collected from two plastic companies in the vicinity of Islamabad, named PP and IP shown in Fig. S1. Three samples have been collected from each industry as replicates. Samples have been collected from the outlet of industrial wastewater effluent during the production time for the detection and quantification of DBP. All the protocols have been followed according to the methods as reported in literature.[34–36] After sample collection, the samples were stored for further analysis to detect phthalates in wastewater and total organic compounds from the solids. Different parameters of wastewater have been evaluated, including total turbidity, pH, total dissolved solids (TDS), electrical conductivity (EC), total suspended solids (TSS), and chemical oxygen demand (COD) (Table S1). For the detection and quantification of di-butyl phthalates, gas chromatography mass spectroscopy (GC-MS) has been performed.

2.4 Characterizations of synthesized materials

X-ray Photoelectron Spectroscopy (XPS) analysis was carried out with a Thermo Scientific ESCALAB 250Xi system equipped with an Al Kα X-ray source to determine the elemental composition and oxidation states of the surface elements. The internal morphology and particle dispersion were examined using Transmission Electron Microscopy (TEM) performed on a Titan ETEM G2 80–300 microscope (FEI Co., USA) operating at 200 kV. Fourier Transform Infrared Spectroscopy (FTIR) was employed to identify and track changes in functional groups, providing insights into chemical interactions and surface modifications. Additionally, UV-Visible Spectroscopy was performed to study the optical absorption properties of the catalysts and to monitor the evolution of degradation intermediates during the treatment process. These combined techniques offered a detailed understanding of the structural integrity of catalyst, composition, morphology and surface chemistry.

2.5 Experimental

2.5.1 Electrode assemblies. The electrocatalytic tests were carried out in a 200 mL electrochemical cell. In the reactor, 1 M Potassium hydroxide (KOH) was used as a supporting electrolyte. Different concentrations of DBP were tested in a 200 mL reactor. A constant current source has been used to provide power to the reactor. A pilot-scale investigation for the treatment of artificially synthesized wastewater has been used in order to evaluate the concentration of DBP and degradation efficiency. Binder was prepared by mixing 20 μL Nafion and 80 μL propanol. Three kinds of electrodes were used during electrochemical reaction measurement, *i.e.*, Reference, working, and counter. Glassy carbon and Ag/AgCl electrodes are used as working and reference electrodes, while the counter

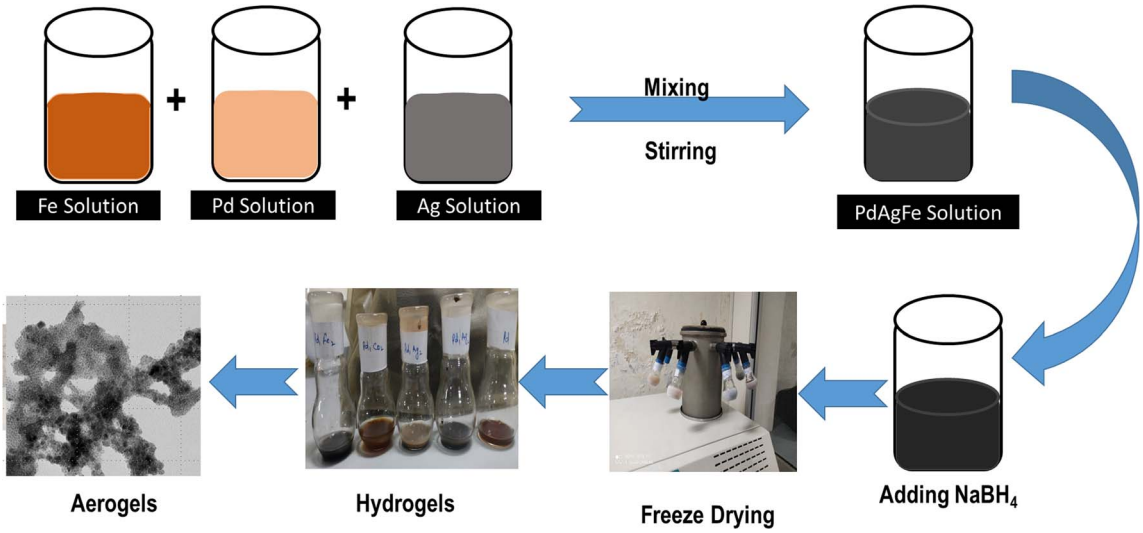

Fig. 1 Schematic diagram of synthesis protocol of palladium-based nano aerogels.

electrode is made of platinum. For testing, 0.002 g of catalyst was dispersed in 100 μL of Nafion and propanol, and the dispersion was ultrasonicated for 20 min. After this, 15 μL catalyst solution was then deposited on the working electrode using a micro pipette and was oven dried at 50 °C for 5 min shown in Fig. S2.

2.5.2 Experimental setup. All electrochemical experiments were conducted using a conventional three-electrode system. A glassy carbon electrode (GCE) coated with the catalyst served as the working electrode, a platinum wire as the counter electrode, and an Ag/AgCl electrode as the reference. The electrolyte solution was 1 M KOH. Electrochemical performance for the degradation of di-butyl phthalate (DBP) was evaluated at three different initial concentrations: 30, 60, and 90 mg L^{-1}. Linear Sweep Voltammetry (LSV) was conducted to assess the oxygen evolution reaction (OER) activity by measuring the current response over applied potential. Electrochemical Impedance Spectroscopy (EIS) was performed over a frequency range of 100 kHz to 0.1 Hz with an amplitude of 5 mV to determine charge transfer resistance. To assess catalyst stability, chronopotentiometric tests were conducted at a constant current density of 5 mA cm^{-2} for 8 hours in the presence of DBP (30, 60, or 90 mg L^{-1}). The change in potential over time was monitored to evaluate catalyst durability and performance under continuous operation. Electrochemical tests were repeated at scan rates of 5, 10, and 15 mV s^{-1} to optimize degradation conditions. All experiments were conducted at ambient temperature, and the electrolyte solution was continuously stirred to maintain homogeneity.

2.6 Analysis

For wastewater characterization, different tests were performed, including Chemical oxygen demand by using the close reflux method (APHA Method No.5220), total suspended solid (TSS) by the Gravimetric method (APHA Method No. 2540 D), electrical conductivity (EC), pH, and total dissolved solids (TDS) by a Multi-meter (Crimson MM 40+) shown in Table S1. Different metals present in the samples were tested and quantified by using Inductively Coupled Plasma Optical Emission Spectrometry (ICP-OES) (5110 ICP-OES, PAK). Different kinds of organics and phthalates were detected by using Gas chromatography mass spectrometer (GC-MS 5977 B AGILENT TECHNOLOGIES USA). LSV, EIS, and chronopotentiometry were performed by CS310M EIS potentiostat/Galvanostat.

3. Results and discussion

3.1 Heavy metal analysis (ICP-OES)

Elemental concentrations of collected wastewater and water samples were analyzed using ICP-OES. The elevated concentrations of some metals in PP, *i.e.*, Aluminum (0.51 mg L^{-1}), Cadmium (0.01 mg L^{-1}), cobalt (0.19 mg L^{-1}) and Iron (2.5 mg L^{-1}), can be due to various reasons shown in Fig. 2. These can be due to the contamination at the time of manufacturing, poor quality raw material used, or inappropriate storage and handling of the PVC. Excessive cadmium concentration can be caused by the use of specific stabilizers or pigments in the production of PVC, while higher iron concentration than the permissible limit is due to raw material impurities or corrosion of equipment.[37] Moreover, low quality control or failure to follow regulatory standards in the manufacturing process may lead to these high metal levels.

3.2 Phthalates analysis (GC-MS)

Gas Chromatography Mass Spectrometry was used to identify the various organics present in the sample (Table S2). In Fig. 3a, Chromatogram shows that di-isooctyl phthalate is the prevailing compound in the sample, with a relative area of 95.90% at a retention time of 22.141 minutes. It is abundant because it is widely used as a plasticizer in the manufacture of flexible polyvinyl chloride (PVC), which is used in products such as flooring, medical equipment, cables, and coatings.[38] The function of di-isooctyl phthalate is to soften and strengthen PVC accounts for its substantial occurrence. Whereas ethylbenzene

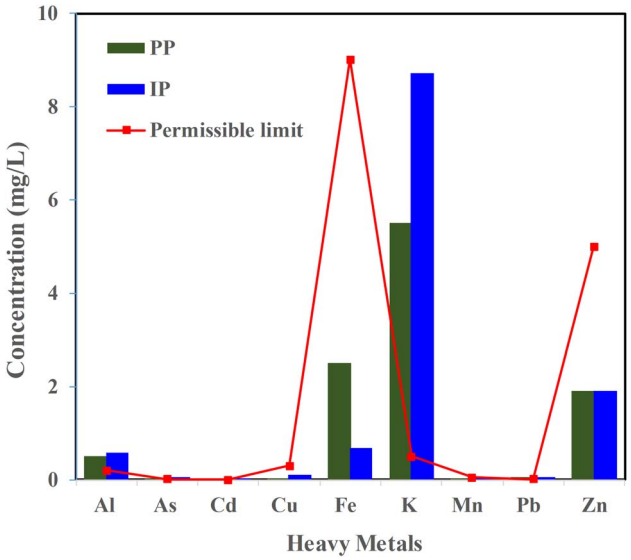

Fig. 2 ICP-OES analysis of wastewater from plastic industries, showing the concentrations of different metals present.

and *p*-xylene occur in considerably lower concentrations, probably as trace contaminants or by-products of the PVC process or related industrial operations. The GC-MS analysis of sample IP in Fig. 3b indicates that di-isooctyl phthalate is the predominant constituent (92.23%), consistent with its widespread use as a plasticizer in PVC-based materials.[39] Minor compounds like ethylbenzene, *p*-xylene, and phenol, 2,4-bis (1,1-dimethylethyl) were identified in trace quantities. The low levels of ethylbenzene and *p*-xylene in the sample result from their high volatility and limited interaction with the polymer matrix. These chemicals have entered the system as solvents or manufacturing byproducts but were largely eliminated by evaporation or heat treatment. Their weak interaction with PVC chains also restricts their retention, resulting in only trace amounts in the finished product. The results confirm that the sample contains typical PVC additives, with potential implications for chemical leaching and environmental impacts.[40]

3.3 Characterization of synthesized materials

3.3.1 Transmission electron microscopy (TEM). Transmission electron microscopy (TEM) was employed to investigate the morphology and structural features of the synthesized PdAgFe, PdAg, and PdFe nano-aerogels obtained *via* freeze-drying (Fig. 4a–f). The selected area electron diffraction (SAED) pattern of the PdAgFe sample (Fig. 4a) displays several concentric diffraction rings, indicating the polycrystalline nature of the material and confirming the presence of a face-centered cubic (fcc) Pd-based alloy structure. Similar diffraction features have been widely reported for Pd-based metallic aerogels, where the interconnected nanoparticle framework consists of multiple nanocrystalline domains rather than single crystals. The TEM image of PdAgFe (Fig. 4b) reveals an interconnected nanoparticle framework of ultrafine particles (3–6 nm), forming a sponge-like porous structure. Such nanoscale networks are characteristic of Pd aerogels formed through nanoparticle gelation, where primary particles of about 3–5 nm assemble into a porous architecture with high surface area.

In comparison, the PdAg aerogel (Fig. 4c and d) shows slightly larger nanoparticles (8–12 nm) forming branched ligaments within a continuous network. Similar morphologies have been reported for Pd–Ag alloy aerogels, in which interconnected nanoparticle chains generate hierarchical porous structures that are beneficial for catalytic activity.[41] The PdFe aerogel (Fig. 4e and f) exhibits relatively larger particle clusters (20–25 nm) with a somewhat denser but still interconnected porous framework. This trend agrees with previous reports indicating that the incorporation of secondary transition metals can influence nucleation and lead to larger particle aggregates in Pd-based aerogels.[33] Overall, all samples display typical interconnected porous aerogel structures composed of crystalline Pd-based nanoparticles, while the PdAgFe aerogel shows the finest nanoparticle distribution, which may provide higher surface area and improved catalytic performance compared with the bimetallic systems.[42]

3.3.2 Fourier transformed infrared spectroscopy (FTIR) and UV-vis spectroscopy. The FTIR spectra in the range of 500–800 cm^{-1} reveal distinct vibrational features for PdFe, PdAgFe, and PdAg electrodes, highlighting differences in their surface

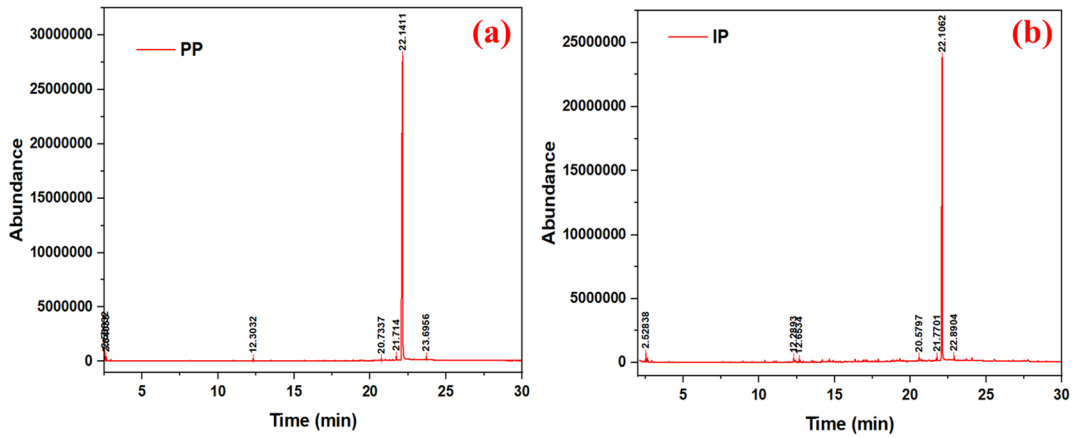

Fig. 3 GC-MS spectra of sample PP (a) and IP (b) for identification of phthalates.

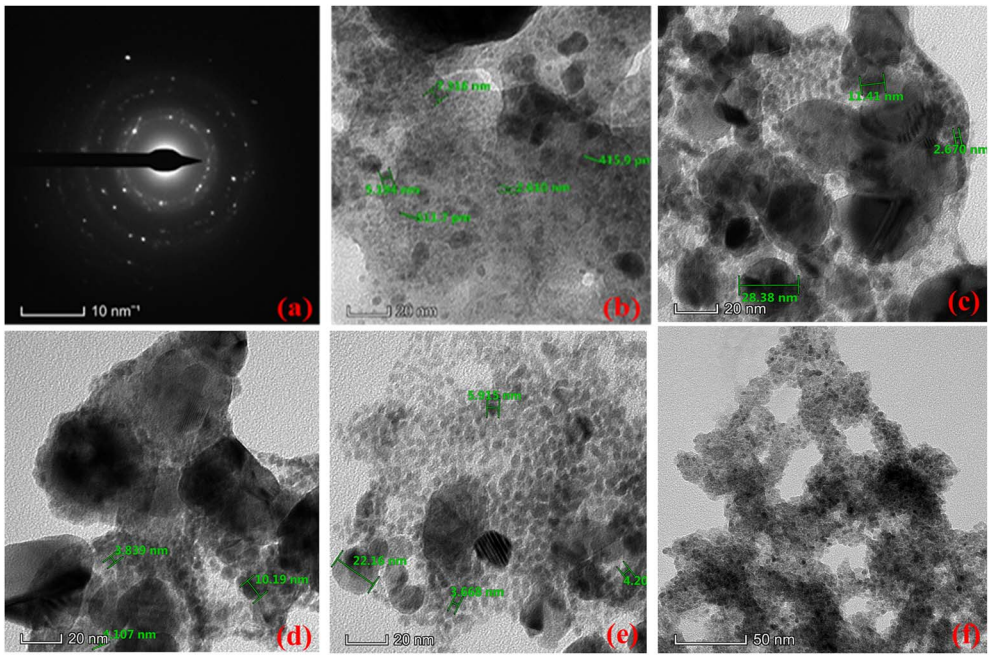

Fig. 4 TEM images of PdAgFe (a and b), PdAg (c and d), and PdFe (e and f) at a resolution of 20 and 50 nm.

chemistry and bonding environments. The PdFe electrode exhibits strong and sharp peaks around 505, 537, and 563 cm^{-1}, characteristic of Fe–O stretching vibrations, suggesting the presence of iron oxide species and high surface reactivity. In contrast, the PdAgFe spectrum shows multiple moderate-intensity peaks at 506, 528, 550, and 584 cm^{-1}, along with additional bands in the 620–660 cm^{-1} range. These indicate a combination of Fe–O, Pd–O, and possibly Pd–Fe or Pd–Ag interactions, confirming the formation of a ternary alloy with synergistic bonding.[43] Meanwhile, the PdAg electrode shows fewer and less intense peaks, mostly between 505 and 570 cm^{-1}, implying limited surface functionalities and weaker metal oxygen bonding shown in Fig. 5a. Overall, the PdAgFe electrode exhibits a more complex and chemically active structure, likely contributing to its superior catalytic performance.[44]

The UV-Vis-NIR transmittance spectra in the range of 400–1000 cm^{-1} reveal distinct optical behaviors for PdAg, PdFe, and PdAgFe electrodes, as demonstrated in Fig. 5b. The UV-Vis spectra show broad absorbance across the 500–1000 nm range. In general, metallic or plasmonic nanoparticles exhibit featureless, rising absorbance into the NIR, whereas semiconducting oxides exhibit a distinct absorption edge at the bandgap. For reference, bulk PdO has a direct bandgap of 2.2 eV (564 nm), so an absorption onset near 560 nm would indicate PdO-like semiconducting behavior. In contrast, silver nanoparticles exhibit a strong surface plasmon resonance (SPR) around 400–420 nm, with a broad tail extending into the visible. In our aerogels, the PdAg and PdAgFe samples display very broad, featureless absorption (no sharp edge) across 500–1000 nm, consistent with metallic alloy/plasmonic behavior. For example, Scanlon *et al.* report that small Ag spheres (10–50 nm) have an SPR near 400 nm, while larger ones (100 nm) shift to 480 nm, and that alloying with Pd produces similarly broad bands. The PdFe aerogel, in contrast, would be expected to show a somewhat steeper rise starting around the PdO bandgap (~2.2 eV) if significant PdO or FeOx is present. Fig. 5b shows a relatively sharper increase in absorbance near 560–600 nm for PdFe *versus* a more gradual increase for PdAg or PdAgFe, this would signal semiconducting character in PdFe (PdO/FeOx bandgap) and more metallic character in PdAg/PdAgFe. This trend agrees with the literature: Pd–Ag alloy nanostructures exhibit broad SPR-derived absorption bands whose positions and widths depend on composition, whereas pure PdO shows an absorption edge at ~2.2 eV. In summary, the UV-Vis data suggest that the PdAgFe and PdAg aerogels behave more like conductive alloys (broad absorption) and the PdFe aerogel shows more oxide-like absorption around the PdO bandgap. These assignments and shifts are consistent with the known optical behavior of PdO and Ag nanoparticles.

Among them, PdAg exhibits the highest transmittance, reaching over 11% at 1000 cm^{-1}, indicating minimal optical absorption and weaker electronic interactions. In contrast, PdFe shows moderate transmittance, rising from 2.5% at 400 to 9% at 1000 cm^{-1}, suggesting increased absorption due to the incorporation of Fe. Notably, the PdAgFe electrode displays the lowest transmittance across the spectrum, starting from 2.3% at 400 cm^{-1} and reaching only 8.8% at 1000 cm^{-1}.[45] This enhanced absorption indicates stronger electronic interactions and greater light-matter coupling, likely due to the synergistic combination of Pd, Ag, and Fe. The lower transmittance of PdAgFe supports its superior electrochemical activity by promoting higher charge carrier generation and transfer efficiency.[46]

3.3.3 X-ray photoelectron spectroscopy (XPS). XPS confirms that the Pd–Ag–Fe catalyst samples contain metallic Pd alloyed with Ag and Fe, with predominantly Pd^0 on the surface and

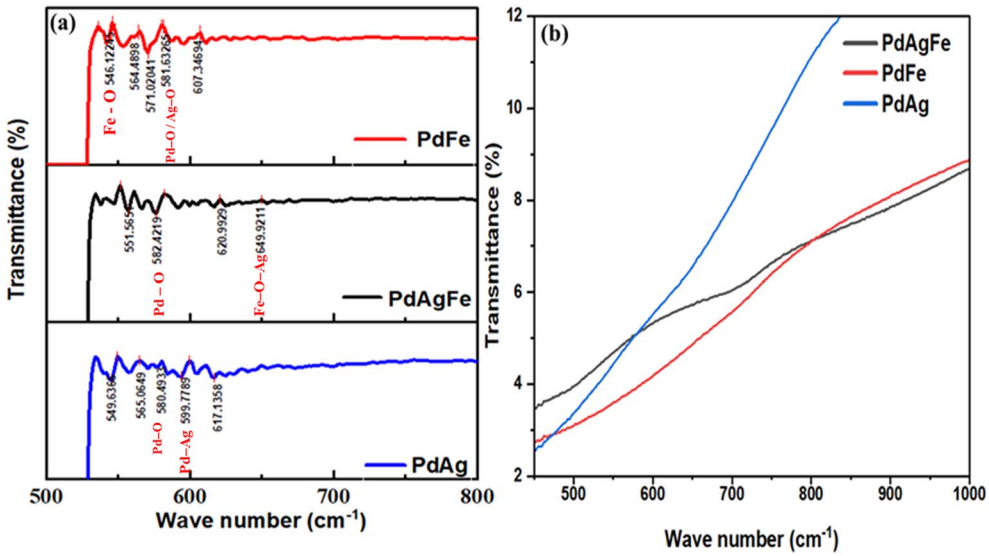

Fig. 5 FTIR (a) and UV-Vis (b) spectra of PdAgFe, PdAg, and PdFe electrocatalysts highlighting characteristic vibrational bands and optical absorption features.

mixed-valence Ag/Fe species. In detail, Fig. 6a shows Pd and Ag peaks in both samples and Fe 2p signals (710–725 eV) only in S5, indicating successful Fe incorporation and slight changes in Pd/Ag intensities. Fig. 6b (Pd 3d of S5 PdAgFe) reveals Pd $3d_{5/2}$ peaks at 334.3 eV and 336.8 eV, assigned to Pd^0 and Pd^II (PdO), with the $3d_{3/2}$ pair at ~339.7 and 343.1 eV. The strong intensity of the Pd^0 peaks shows that surface Pd is largely metallic.[47] Fig. 6c (Pd 3d of PdAg sample) shows Pd^0 at 332.9/340.8 eV and Pd^II at 335.5/343.4 eV, consistent with reference Pd^0 (~335.0 eV) and Pd^II (~336.7 eV). The 2 eV lower Pd^0 BE in PdAg reflects alloying (electron donation from Ag to Pd). Fig. 6d (Ag 3d of PdAgFe) shows Ag $3d_{5/2}$ peaks at 366.97 eV (higher-valent Ag, labeled Ag^III) and 367.75 eV (Ag^I/Ag^0), with $3d_{3/2}$ at 372.76 eV and a satellite at 373.21 eV. For comparison, Ag^0 is 368.2/374.2 eV; the observed 0.3–0.5 eV downshift and loss satellite are characteristic of partially oxidized Ag and plasmon shake-up. Fig. 6e (Fe 2p of PdAgFe) shows Fe $2p_{3/2}$ at 711.8 eV and 713.3 eV, assigned to Fe^II and Fe^III, with Fe $2p_{1/2}$ ~725 eV and a shake-up at 733.3 eV, consistent with mixed Fe^2+/Fe^3+ oxides.[48] The high-resolution spectra show that metallic Pd^0 dominates (with only minor PdO), while Ag and Fe appear in oxidized states. The slight BE shifts of Pd and Ag peaks (*versus* bulk references) indicate alloying/charge-transfer effects, and the shake-up satellites confirm the presence of oxidic species. In this case the Fe can as an electron mediator and improve the formation of reactive oxidative species, thus refining the electrocatalytic efficiency of the system. Overall, the XPS data support a Pd–Ag–Fe alloy surface: abundant metallic Pd with some oxide, electronic Pd–Ag–Fe interactions (*via* charge transfer), and Fe/Ag oxide species. Introducing Ag and Fe into Pd alloys shifts electron density onto Pd, making Pd atoms more negatively charged. This increases Pd screening of its core electrons and lowers the Pd $3d_{5/2}$ XPS binding energy by a few tenths of an eV. Mechanistically, electronegativity-driven charge transfer (Ag → Pd, Fe → Pd), alloy ligand effects, and strain (from Fe) enrich Pd in d-electrons. This enrichment moves Pd's d-band center downward (toward the Fermi level) and lowers its work function, weakening adsorption of *CO, *H, *O, *OH on Pd sites. These features (Pd–Ag electron modification of the Pd d-band and mixed-valence surface species) are expected to tune the catalyst's adsorption properties and enhance its selectivity and thermal stability (preventing overoxidation or sintering), consistent with improved catalytic.[49,50]

3.4 Electrochemical testing

3.4.1 Linear sweep voltammetry. The LSV curves of PdAgFe, PdFe, and PdAg at scan rates of 5, 10, and 15 mV s^{-1} illustrate their electrocatalytic performance toward the oxygen evolution reaction (OER) in alkaline medium. Among the three, PdAgFe exhibits the lowest onset potential of 1.39 V, Fig. 7a, compared to 1.55 V, Fig. 7b, for PdFe and 1.57 V for PdAg, Fig. 7c, indicating it initiates the OER at a lower applied voltage. Correspondingly, PdAgFe shows the lowest overpotential of 160 mV, while PdFe and PdAg exhibit higher overpotentials of 320 mV and 340 mV, respectively. These values highlight the superior catalytic efficiency of PdAgFe, which requires significantly less energy to drive water oxidation.[25] This enhanced performance is attributed to improved charge transfer and synergistic effects among Pd, Ag, and Fe in the trimetallic structure, positioning PdAgFe as the most promising catalyst for water splitting applications.

$$E_{RHE} = E_{Ag/AgCl} + 0.197\ V + 0.0591\ V \times pH,$$

This formula (Nernst relation for RHE) is now stated in the Experimental section for completeness, and we cite a recent source for it.

The LSV measurements were carried out to evaluate the Oxygen Evolution Potential (OEP) of various electrodes in a 1 M

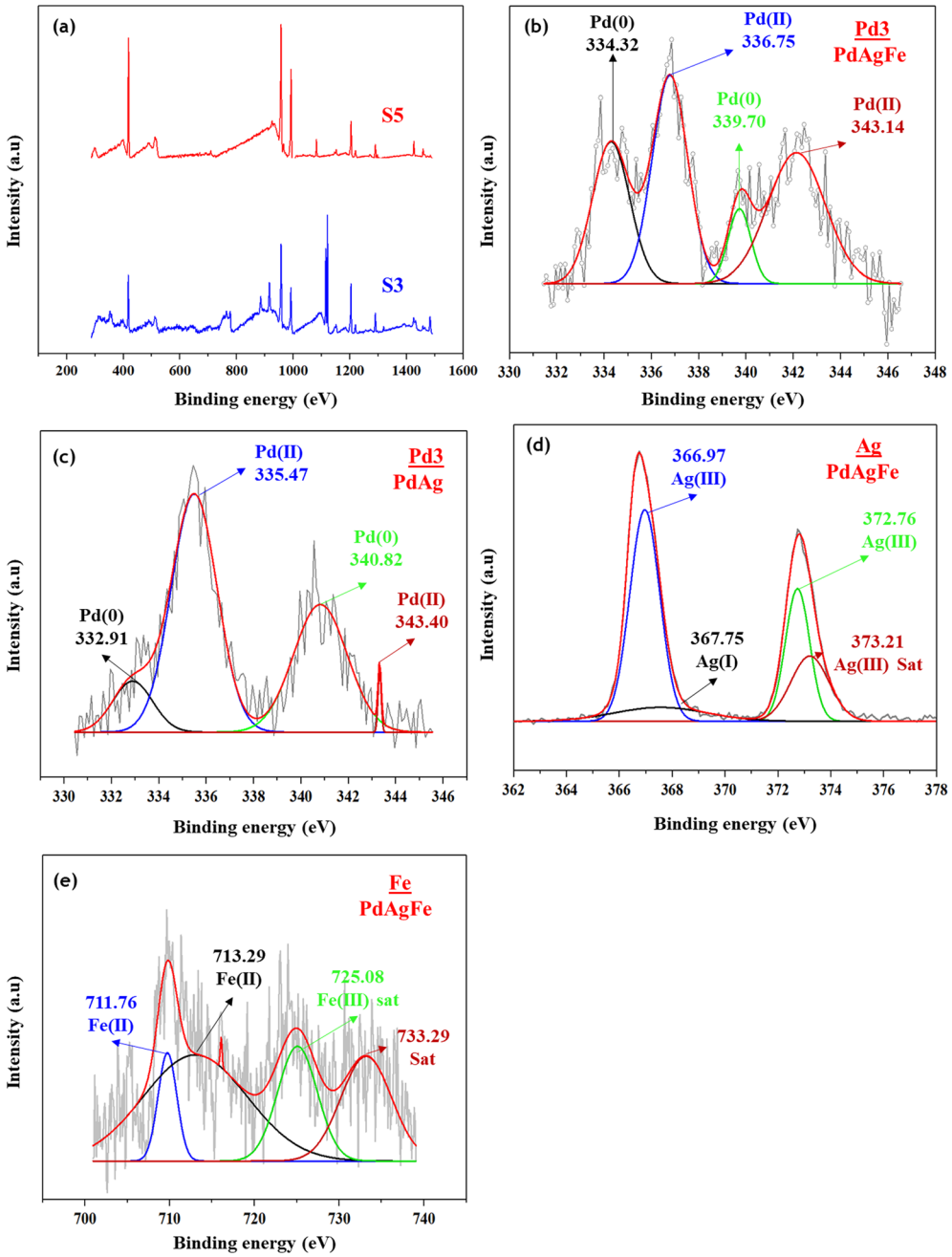

Fig. 6 X-ray photoelectron spectroscopy (XPS) analysis of PdAg and PdAgFe electrocatalysts. (a) Survey spectra showing the elemental composition of PdAg and PdAgFe. High-resolution spectra of Pd 3d for PdAg (b) and PdAgFe (e). High-resolution Ag 3d spectra for PdAg (c) and PdAgFe (d). (e) High-resolution Fe 2p spectrum of PdAgFe, confirming the presence of Fe species.

KOH solution under ambient conditions with a scan rate of 5 mV s^{-1}. As shown in Fig. 7d, at a DBP concentration of 30 mg L^{-1}, the PdAgFe electrode exhibits the highest OEP of 1.61 V (*vs.* Ag/AgCl), approximately 40% higher than that of the PdAg electrode and 18% higher than that of the PdFe electrode. This indicates that the ternary composition of Pd, Ag, and Fe significantly enhances the electrochemical oxidation potential. In Fig. 7e, where the DBP concentration increases to 60 mg L^{-1}, the PdAgFe electrode again shows superior performance with an OEP of 1.70 V. This value is 28% higher than that of PdAg and 8% higher than PdFe, maintaining its advantage as pollutant concentration increases.[51]

Further, in Fig. 7f at the highest DBP concentration of 90 mg L^{-1}, the PdAgFe electrode achieves an OEP of 1.97 V, which is 43% higher than PdAg and 20% higher than PdFe. The consistent rise in OEP with increasing pollutant concentration suggests that more organic molecules compete with water for oxidation, thereby suppressing the oxygen evolution reaction (OER) and allowing for more efficient pollutant degradation.[52] Higher OEP reduces energy loss due to premature oxygen evolution and improves selectivity for organic oxidation.

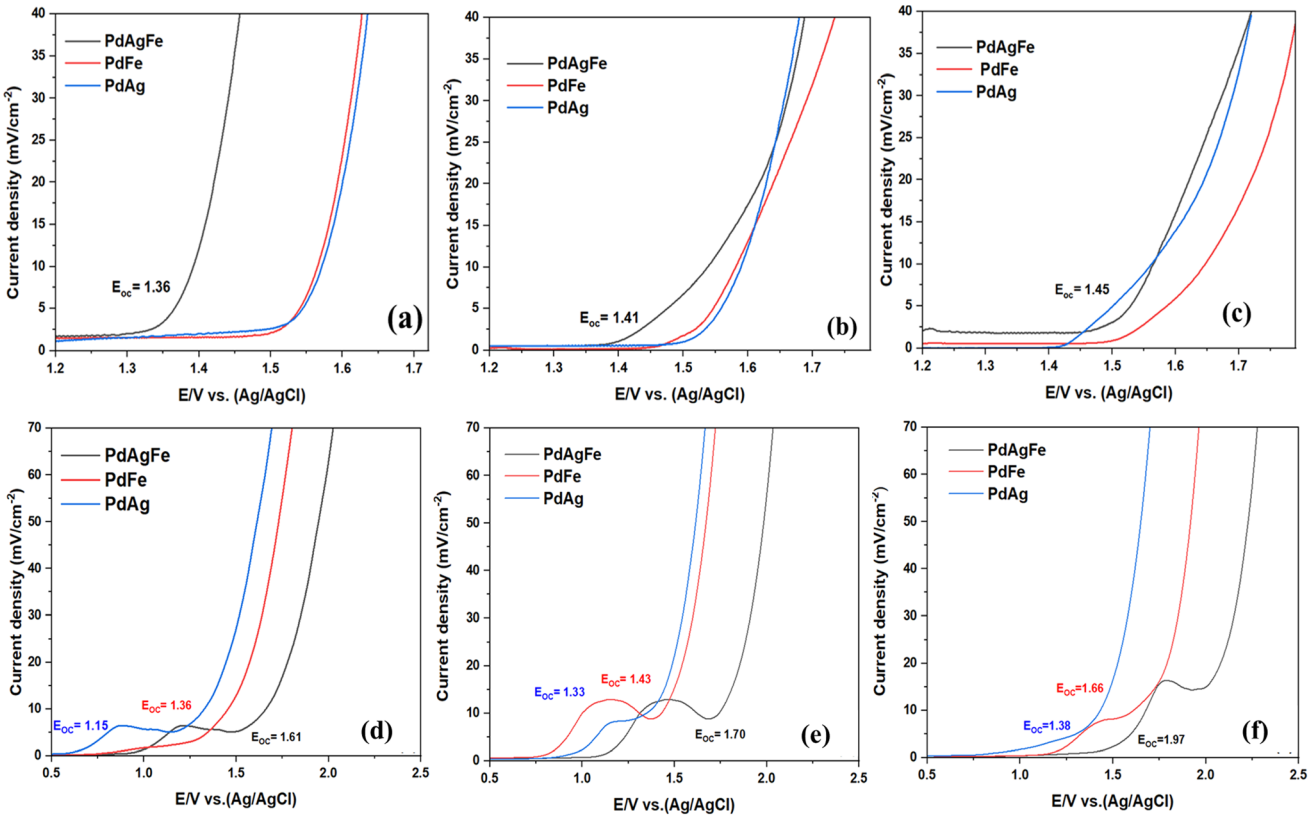

Fig. 7 Oxygen evolution reaction (OER) polarization curves of PdAg, PdFe, and PdAgFe electrocatalysts recorded at scan rates of 5 mV s^{-1} (a), 10 mV s^{-1} (b), and 15 mV s^{-1} (c) in 1 M KOH electrolyte. Linear sweep voltammetry (LSV) curves for OER using the same electrocatalysts at a scan rate of 5 mV s^{-1} in 1 M KOH in the presence of DBP, evaluated at initial concentrations of 30 mg L^{-1} (d), 60 mg L^{-1} (e), and 90 mg L^{-1} (f).

Therefore, the PdAgFe electrode offers superior electrocatalytic performance, particularly at higher pollutant concentrations, making it the most effective among the tested materials.

The anodic peaks observed in the LSV curves (Fig. 7d–f) are attributed to the electrochemical oxidation of DBP and its intermediate products in alkaline medium. At lower potentials, the current response corresponds to the direct oxidation of DBP involving dealkylation and hydroxylation pathways, forming intermediates such as mono-butyl phthalate and phthalic acid, as reported in previous electrochemical degradation studies of phthalate. The higher current density observed for PdAgFe suggests enhanced catalytic activity due to synergistic electronic interactions among Pd, Ag, and Fe. At more positive potentials, the sharp increase in current is associated with the oxygen evolution reaction (OER), which becomes dominant once organic oxidation is kinetically limited. This behavior is consistent with electrochemical advanced oxidation processes reported in alkaline media.[53–55]

Lower E_{onset} in blank electrolyte means the catalyst is intrinsically more active for OER (lower overpotential). Higher OEP in the presence of organics means that water oxidation is suppressed to a higher potential, indicating that charge is instead used for oxidizing the organics (*i.e.* better selectivity). This inverse relationship has been noted: a higher OEP corresponds to poorer OER activity (which is actually beneficial for organic oxidation).[56] We have added this point, citing that "the higher the OEP is, the worse the OER activity is conducive to acquiring higher current efficiency.[57,58]

3.4.2 COD removal. The COD removal performance of PdAgFe, PdFe, and PdAg electrodes was evaluated at DBP concentrations of 30 mg L^{-1}, 60 mg L^{-1}, and 90 mg L^{-1}. At 30 mg L^{-1} shown in Fig. 8a the initial COD was approximately 120 mg L^{-1}. After 8 hours, PdAgFe reduced the COD to around 2 mg L^{-1}, while PdFe and PdAg reached approximately 10 mg L^{-1} and 27 mg L^{-1}, respectively. At 60 mg L^{-1}, Fig. 8b with an initial COD of about 140 mg L^{-1}, PdAgFe again showed the best performance, lowering COD to about 3 mg L^{-1}, followed by PdFe at 16 mg L^{-1} and PdAg at 44 mg L^{-1}. At the highest concentration of 90 mg L^{-1} Fig. 8c initial COD of 160 mg L^{-1} PdAgFe, reduced COD to 5 mg L^{-1}, PdFe to 22 mg L^{-1}, and PdAg to 47 mg L^{-1}. These results clearly indicate that PdAgFe is the most effective electrode across all concentrations, maintaining low final COD values even at higher pollutant loads.[59]

3.4.3 Electrocatalytic removal of DBP. The degradation efficiency of PdAgFe, PdFe, and PdAg electrodes at DBP concentrations of 30 mg L^{-1}, 60 mg L^{-1}, and 90 mg L^{-1} is shown in Fig. 8d. At 30 mg L^{-1} initial COD 120 mg L^{-1}, PdAgFe reduced COD to 2 mg L^{-1} after 8 hours, achieving a 98.3% removal, compared to 91.7% for PdFe and 77.5% for PdAg Fig. 9d. At 60 mg L^{-1} (initial COD 140 mg L^{-1}), PdAgFe again showed the highest efficiency, reaching 3 mg L^{-1} COD 97.9%

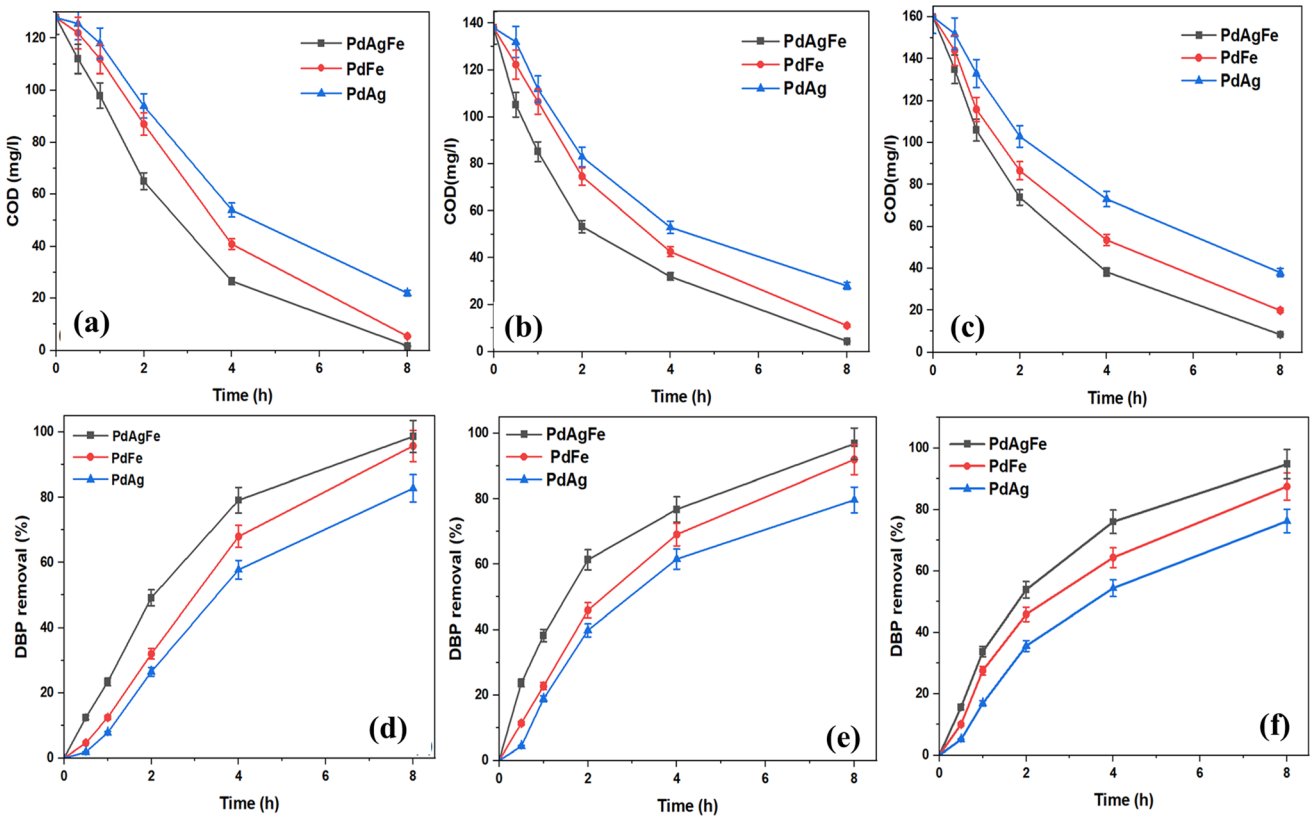

Fig. 8 COD removal efficiencies for DBP at initial concentrations of 30 mg L^{-1} (a), 60 mg L^{-1} (b), and 90 mg L^{-1} (c), followed by DBP removal percentages at 30 mg L^{-1} (d), 60 mg L^{-1} (e), and 90 mg L^{-1} (f) over time using PdAgFe, PdAg, and PdFe electrocatalysts.

removal, outperforming PdFe 88.6% and PdAg (68.6%), Fig. 8e. At 90 mg L^{-1} initial COD (160 mg L^{-1}), PdAgFe reduced COD to 5 mg L^{-1}, 96.9% removal, while PdFe and PdAg achieved 86.3% and 70.6%, respectively. Across all concentrations, PdAgFe consistently showed the highest COD removal, with its performance advantage increasing at higher pollutant loads Fig. 8f. This is attributed to the synergistic effect of the Pd–Ag–Fe combination, which enhances catalytic activity and suppresses undesired oxygen evolution. The rising OEP of PdAgFe with pollutant concentration (from 1.61 to 1.97 V) further supports its superior selectivity and energy efficiency, confirming it as the most effective electrode for DBP degradation. The efficiency of the PdAgFe has been compared with other electrodes for degradation of DBP as summarized in Table 1.

3.4.4 Kinetics. Kinetic plots of the electrocatalytic degradation of COD are presented in Fig. 9. The degradation of COD in the presence of PdAgFe, PdFe and PdAg was examined using the zero-order and pseudo-first-order kinetics using the following equations, respectively.

$$C_0 - C = K_{app}t$$

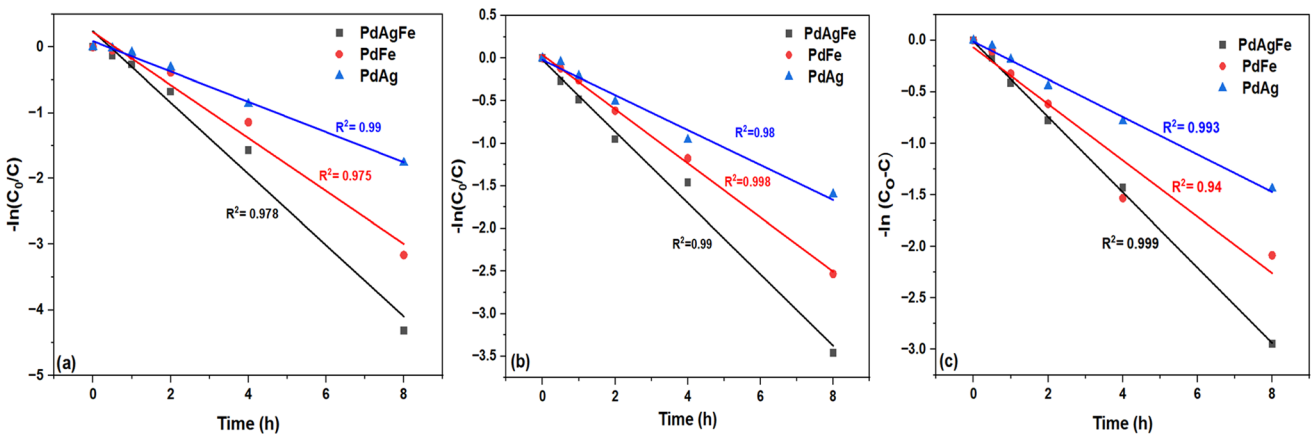

Fig. 9 Pseudo-first order kinetics of COD removal by PdAgFe, PdFe, and PdAg electrocatalyst at 30 mg L^{-1} (a), 60 mg L^{-1} (b), and 90 mg L^{-1} (c).

Table 1 Comparison of PdAgFe with other electrocatalyst for degradation of DBP

Electrocatalyst/System	Operating conditions	DBP removal (%)	Reaction time	References
PdAgFe	90 ppm, 50 m mA cm^{-2} current density, 1 M KOH & 0.05 M Na_2SO_4	98% of DBP	8 h	Present study
IrO_2–Ta_2O_5/Ti electrode	10 V cm^{-1}, 0.005 M Na_2SO_4 60 mg L^{-1} 60 min	90%	1 h	60
Ce-doped Ti/PbO_2 electrode	25 mA cm^{-2}, 0.05 M Na_2SO_4	98.2%	10 h	25
Ti/TiO_2NT with ZrO_2 (photo electrocatalysis)	6 ppm of DBP bias potential of 1.5 V, 0.1 M Na_2SO_4	91%	1.5 h	61
Vanadium pentoxide (V_2O_5) and carbon-coated titanium (C/Ti) (photo electrocatalysis)	75 mg L^{-1} DBP 112 mA cm^{-2} current density, 50 mg L^{-1} catalyst dosage	99.5% of DBP	3.5 h	24

$$-\ln(C_0C) = K_{app}t$$

where C_0 and C are the final and initial concentrations of *vs.* and COD, respectively. K_{app} is the rate constant (min^{-1}).

3.4.5 Pseudo first order kinetics. In Pseudo First-Order Kinetics of PdAgFe, PdFe, and PdAg, PdAgFe consistently delivers the best performance in both degradation rate and conformity to first-order kinetics. At 30 mg L^{-1} COD, PdAgFe shows the highest rate constant of 0.54 h^{-1}, followed by PdFe at 0.40 h^{-1}, while PdAg, although showing the best kinetic fit, has the lowest rate constant of 0.23 h^{-1}, Fig. 9a. At 60 mg L^{-1}, PdAgFe again outperforms the others with a rate constant of 0.419 h^{-1} and an excellent R^2 of 0.998. PdFe and PdAg follow with rate constants of 0.31 h^{-1} and 0.20 h^{-1} respectively, Fig. 9b. At 90 mg L^{-1}, PdAgFe maintains its superiority with a rate constant of 0.36 h^{-1}, PdFe shows a moderate rate of 0.27 h^{-1} while PdAg again displays the lowest rate, 0.18 h^{-1}, despite a strong R^2 of 0.993, Fig. 9c. Overall, PdAgFe proves to be the most efficient and reliable catalyst across all concentrations, combining high degradation rates with excellent adherence to first-order kinetics. In zero-order kinetics, PdFe shows relatively good linearity with R^2 values of 0.95 and 0.91 at 30 and 60 mg L^{-1}, while PdAgFe gives 0.85 at 90 mg L^{-1}. However, the overall fit is weaker than in pseudo-first-order kinetics, confirming that the reaction follows first-order behavior more reliably.

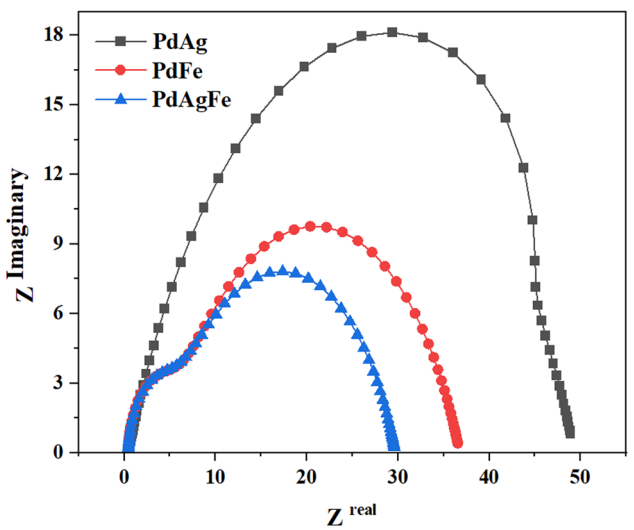

Fig. 10 Electrochemical impedance spectroscopy of PdAg, PdFe, and PdAgFe.

3.5 Electrochemical impedance spectroscopy

The Nyquist plot depicts the electrochemical impedance response of PdAg, PdFe, and PdAgFe electrodes, characterized by semicircular arcs typically associated with charge transfer resistance at the electrode–electrolyte interface. The PdAg electrode exhibits the largest semicircle, corresponding to the highest charge transfer resistance, indicative of sluggish charge transfer kinetics shown in Fig. 10. In contrast, the PdAgFe electrode displays the smallest arc, reflecting the lowest resistance and enhanced charge transfer efficiency. The PdFe electrode shows intermediate impedance behavior. The reduced impedance in the PdAgFe system suggests a synergistic interaction among Pd, Ag, and Fe, likely enhancing the electronic conductivity of material and catalytic activity. These results highlight the potential of the PdAgFe ternary alloy for high-performance electrochemical applications.

4. Limitations and challenges

Although Pd usage was reduced, the catalyst still contains precious metals. Advanced electrodes like Pd-based aerogels can be expensive relative to conventional materials, and their synthesis (*e.g.* sol–gel and supercritical drying for aerogels) may not easily scale to large size. Indeed, high electrode cost and fabrication complexity are known barriers to large-scale electrochemical treatment. Moreover, freestanding aerogel structures can be mechanically fragile (similar to issues with boron-doped diamond substrates) so ensuring structural durability in real reactors is a challenge. The experiments were performed in controlled, pure-DBP solutions. In real wastewater or surface waters, competing ions and natural organic matter can alter performance. In particular, chloride or bromide ions may form chlorine or bromine radicals and generate toxic byproducts (chlorates, bromates, or halogenated organics) during electrooxidation. While the study calls for lower current densities, the high operating voltage suggests that further

optimization of cell design is needed. High energy demand could offset the catalyst's benefits unless addressed.

5. Conclusions

This study revealed the successful integration of transition metals Ag and Fe with Pd aerogels as an efficient and economically feasible electrocatalyst. The result demonstrated outstanding electrocatalytic performance, achieving 98.3% DBP removal at a high pollutant concentration (90 ppm), lower current density (160 mV), and higher OEP (1.97 V) than PdAg and PdFe. By alloying Pd with Ag and Fe, the catalyst retained high activity while greatly reducing Pd content, offering a more cost-effective alternative to pure-Pd electrodes. Importantly, unlike many adsorbents that merely concentrate DBP (often leaving most of the organic load behind), the PdAgFe system drove considerable mineralization of the pollutant, as showed by significant COD reduction, indicating a high degree of oxidation. These results position PdAgFe among the state-of-the-art electrocatalysts for DBP removal and highlight its promise for water treatment applications.

Future work should evaluate PdAgFe electrodes in actual water samples containing DBP (and other species). This includes spiking municipal or industrial wastewater with DBP at microgram-*per*-liter levels to monitor removal and to screen for any harmful byproducts (*e.g.*, chlorinated organics or perchlorates). The system should be redesigned to lower power consumption while maintaining high removal rates. Strategies include reducing the inter-electrode distance, using pulsed or dynamic operation, and increasing catalyst loading or surface area to allow lower current density for the same throughput. Literature on electrooxidation suggests that operating at moderate current densities (*e.g.*, 100–300 A m^{-2}) can control toxic byproducts but still achieve oxidation. Develop scalable synthesis routes for PdAgFe catalysts. For example, electro-depositing the Pd–Ag–Fe alloy onto conductive substrates (carbon paper or metal foam) could yield robust catalyst layers without the need of delicate drying. Alternatively, templated methods (freeze-casting, 3D printing) might produce porous structures at scale. Mechanical reinforcement (*e.g.* embedding the aerogel in a composite matrix) could prevent crumbling under flow. Pilot-scale trials with larger electrode assemblies should be pursued to identify engineering challenges.

Conflicts of interest

The authors declare that the research was conducted in the absence of any commercial or financial relationships that could be construed as a potential conflict of interest.

Data availability

The data supporting the findings of this study, including electrochemical testing and material characterization data (both raw and processed), are not currently deposited in a public repository but are available from the corresponding author, Muzammil Anjum (muzammilanjum@gmail.com; muzammilanjum@uaar.edu.pk), or the first author upon reasonable request.

Supplementary information (SI) is available. See DOI: https://doi.org/10.1039/d6ra00270f.

Acknowledgements

This work was funded and supported under the project No. 16476 (2022–2025) funded by Higher Education Commission of Pakistan under National Research Program for Universities (NRPU).

References

1 S. Khurshid, M. Anjum, R. Nawaz, F. Kauser, S. Saleem, M. M. Hanafiah and M. Abbas, *Environ. Geochem. Health*, 2025, **47**(9), DOI: 10.1007/s10653-025-02707-2.
2 D. Ding, Y. Wang, J. He, J. Gao, Z. Xu, Y. Dou, L. Guo, X. Ji, M. Shu and T. Yue, *Environ. Toxicol. Chem.*, 2025, **44**, 1165–1186.
3 M. C. Schilling Costello, N. Asad, M. Haris, P. Yousefi, B. Khan and L. S. Lee, *Environ. Toxicol. Chem.*, 2023, **42**, 2599–2613.
4 G. Abdul, X. Zhu and B. Chen, *Chem. Eng. J.*, 2017, **319**, 9–20.
5 W. Shuai, C. Gu, G. Fang, D. Zhou and J. Gao, *J. Environ. Sci. (China)*, 2019, **80**, 5–13.
6 A. Tuli, G. Suresh, N. Halder and T. Velpandian, *Environ. Sci. Pollut. Res.*, 2024, **31**, 23408–23434.
7 D. Liao, F. Wu, T. Deng, F. Yin, P. Su and D. Feng, *Water. Air. Soil Pollut.*, 2024, **235**(5), DOI: 10.1007/s11270-024-07051-2.
8 H. Mou, H. Yang, S. Qu, A. Yang and X. Hu, *Process Saf. Environ. Prot.*, 2025, **194**, 119–128.
9 C. W. Huang, B. S. Nguyen, J. C. S. Wu and V. H. Nguyen, *Int. J. Hydrogen Energy*, 2020, **45**(36), DOI: 10.1016/j.ijhydene.2019.08.121.
10 P. Ganesan, A. Sivanantham and S. Shanmugam, *ACS Appl. Mater. Interfaces*, 2017, **9**, 12416–12426.
11 A. Dutta, R. Adhikary, P. Broekmann and J. Datta, *Appl. Catal. B Environ.*, 2012, **116**(49), DOI: 10.1016/j.apcatb.2019.117847.
12 M. Wu, G. Zhang, J. Qiao, N. Chen, W. Chen and S. Sun, *Nano Energy*, 2019, **61**, 86–95.
13 K. Liu, F. Wang, T. A. Shifa, Z. Wang, K. Xu, Y. Zhang, Z. Cheng, X. Zhan and J. He, *Nanoscale*, 2017, **9**, 3995–4001.
14 D. Yang, L. Cao, L. Feng, J. Huang, K. Kajiyoshi, Y. Feng, Q. Liu, W. Li, L. Feng and G. Hai, *Appl. Catal. B Environ.*, 2019, **257**, DOI: 10.1016/j.apcatb.2019.117911.
15 J. Wang and F. Ciucci, *Appl. Catal. B Environ.*, 2019, **254**, 292–299.
16 L. Li, Z. Deng, L. Yu, Z. Lin, W. Wang and G. Yang, *Nano Energy*, 2016, **27**, 103–113.
17 A. Cuña, C. Reyes Plascencia, E. L. da Silva, J. Marcuzzo, S. Khan, N. Tancredi, M. R. Baldan and C. de Fraga Malfatti, *Appl. Catal. B Environ.*, 2017, **202**, 95–103.
18 B. Cai and A. Eychmüller, *Adv. Mater.*, 2018, **31**(31), DOI: 10.1002/adma.201804881.

19 S. Lai, C. Lv, S. Chen, P. Lu, X. She, L. Wan, H. Wang, J. Sun, D. Yang and X. Zhao, *J. Alloys Compd.*, 2020, **817**, DOI: 10.1016/j.jallcom.2019.152727.
20 S. Li, X. Zheng, H. Jin, L. Qian, K. Wang, Y. Shen, M. Zhao and R. Liu, *Chem. Eng. J.*, 2023, **463**, DOI: 10.1016/j.cej.2023.142367.
21 Y. Zhang, Y. Li, Z. Yao, J. Wang and Q. Zhong, *Int. J. Hydrogen Energy*, 2022, **47**, 6996–7004.
22 Y. Yang, H. Huang, B. Shen, L. Jin, Q. Jiang, L. Yang and H. He, *Inorg. Chem. Front.*, 2020, **7**, 700–708.
23 D. Deng, X. Wu, M. Li, S. Qian, B. Tang, S. Wei and J. Zhang, *Chemosphere*, 2020, **259**, DOI: 10.1016/j.chemosphere.2020.127488.
24 S. Farissi, K. A. Akhilghosh, A. Muthukumar and M. Muthuchamy, *Environ. Technol.*, 2025, **46**, 494–508.
25 Y. Chen, D. Liao, Y. Lin, T. Deng, F. Yin, P. Su and D. Feng, *Chemosphere*, 2022, **288**, DOI: 10.1016/j.chemosphere.2021.132638.
26 N. Maity, A. Mishra, S. Barman, S. K. Padhi, B. B. Panda, E. A. Jaseer and M. Javid, *ACS Omega*, 2024, **9**, 1020–1028.
27 M. Wen, K. Mori, Y. Futamura, Y. Kuwahara, M. Navlani-García, T. An and H. Yamashita, *Sci. Rep.*, 2019, DOI: 10.1038/s41598-019-52133-5.
28 L. Ndlwana, K. Sikhwivhilu, R. M. Moutloali and J. C. Ngila, *Membranes*, 2020, **10**, 1–17.
29 M. Luo and S. Guo, *Nat. Rev. Mater.*, 2017, **02**(11), DOI: 10.1038/natrevmats.2017.59.
30 L. Trotochaud, S. L. Young, J. K. Ranney and S. W. Boettcher, *J. Am. Chem. Soc.*, 2014, **136**, 6744–6753.
31 A. Chen and P. Holt-Hindle, *Chem. Rev.*, 2010, **110**, 3767–3804.
32 A. C. Pierre and G. M. Pajonk, *ChemInform*, 2003, **102**(11), DOI: 10.1002/chin.200304237.
33 A. Martínez-Lázaro, M. H. Rodriguez-Barajas, N. Rey-Raap, F. I. Espinosa, L. Álvarez-Contreras, J. Ledesma-García, A. Arenillas and L. G. Arriaga, *Mater. Today Nano*, 2023, **22**, DOI: 10.1016/j.mtnano.2023.100308.
34 M. Akkbik, V. A. Turksoy and S. Koçoğlu, *Toxicol. Mech. Methods*, 2020, **30**, 33–38.
35 N. G. Gurudatt, K. Lee, W. Heo and H. Il Jung, *Analyst*, 2022, **147**, 3525–3533.
36 M. Zhang, Y. Liu, D. Li, X. Cui, L. Wang, L. Li and K. Wang, *Energies*, 2023, **16**(4), DOI: 10.3390/en16041599.
37 R. Shrestha, S. Ban, S. Devkota, S. Sharma, R. Joshi, A. P. Tiwari, H. Y. Kim and M. K. Joshi, *J. Environ. Chem. Eng.*, 2021, DOI: 10.1016/j.jece.2021.105688.
38 T. Andjelković, D. Bogdanović, I. Kostić, G. Kocić, G. Nikolić and R. Pavlović, *Environ. Sci. Pollut. Res.*, 2021, **28**, 31380–31390.
39 I. Kerienė and A. Maruška, *Urban Water J.*, 2022, **19**, 769–781.
40 S. Bhogal, A. Grover and I. Mohiuddin, *Crit. Rev. Anal. Chem.*, 2024, **54**, 3428–3452.
41 A. Shafaei Douk and H. Saravani, *ACS Omega*, 2020, **5**, 22031–22038.
42 Z. Sun, J. Pan, W. Chen, H. Chen, S. Zhou, X. Wu, Y. Wang, K. Kim, J. Li, H. Liu, Y. Yuan, J. Wang, D. Su, D. L. Peng and Q. Zhang, *Adv. Energy Mater.*, 2023, **14**(02), DOI: 10.1002/aenm.202303165.
43 D. Pércsi, A. Forgács, T. Fodor, I. Fábián, J. Kalmár and P. Herman, *ACS Appl. Nano Mater.*, 2024, **7**, 14629–14640.
44 H. Mansouri-Torshizi, E. Rezaei, F. Kamranfar and M. H. Majd, *Adv. Pharm. Bull.*, 2016, **6**, 449–453.
45 Y. Bazeľ, V. Sidey, M. Fizer, O. Fedyshyn, V. Vojteková, K. Reiffová, Y. Ostapiuk and O. Tymoshuk, *J. Mol. Struct.*, 2021, **1246**, DOI: 10.1016/j.molstruc.2021.131150.
46 S. M. Ali, M. A. M. Khan and T. S. ALKhuraiji, *J. Mater. Sci. Mater. Electron.*, 2020, **31**, 14901–14911.
47 J. Patarroyo, J. A. Delgado, F. Merkoçi, A. Genç, G. Sauthier, J. Llorca, J. Arbiol, N. G. Bastus, C. Godard, C. Claver and V. Puntes, *Sci. Rep.*, 2019, DOI: 10.1038/s41598-019-55105-x.
48 L. Li, P. Ma, S. Hussain, L. Jia, D. Lin, X. Yin, Y. Lin, Z. Cheng and L. Wang, *Sustain. Energy Fuels*, 2019, **3**, 1749–1756.
49 B. Yao, J. Ye, C. Wang, W. Mu, F. Liu and D. Wen, *Appl. Surf. Sci.*, 2023, **631**, DOI: 10.1016/j.apsusc.2023.157540.
50 M. H. Rodríguez-Barajas, A. Gutiérrez, A. Martínez-Lázaro, F. I. Espinosa-Lagunes, N. Rey-Raap, A. Arenillas, J. Ledesma-García and L. G. arriaga, *J. Alloys Compd.*, 2023, **969**, DOI: 10.1016/j.jallcom.2023.172390.
51 P. Zhang, X. Gu, N. Qin, Y. Hu, X. Wang and Y. nan Zhang, *J. Hazard. Mater.*, 2022, **441**, DOI: 10.1016/j.jhazmat.2022.129896.
52 L. Mais, S. Palmas, M. Mascia and A. Vacca, *Catalysts*, 2021, **11**(08), DOI: 10.3390/catal11080882.
53 M. Panizza and G. Cerisola, *Environ. Sci. Technol.*, 2004, **38**, 5470–5475.
54 C. A. Martínez-Huitle and E. Brillas, *Appl. Catal. B Environ.*, 2009, **87**, 105–145.
55 F. C. Moreira, R. A. R. Boaventura, E. Brillas and V. J. P. Vilar, *Appl. Catal. B Environ.*, 2017, **202**, 217–261.
56 C. Batchelor-McAuley, *Curr. Opin. Electrochem.*, 2022, DOI: 10.1016/j.coelec.2022.101176.
57 W. Li, C. Yu, X. Song, Y. Zhang, X. Tan, W. Yang, W. Liu, Y. Yang and J. Qiu, *Nat. Commun.*, 2025, **15**, DOI: 10.1038/s41467-025-63009-w.
58 H. Guo, W. Hu, D. Yang, D. Wan, H. Xu, W. Yan and X. Jin, *Curr. Opin. Electrochem.*, 2023, **37**, DOI: 10.1016/j.coelec.2022.101205.
59 S. Farissi, S. Ramesh, A. A. Gado, P. Tejomurtula, A. Muthukumar and M. Muthuchamy, *J. Appl. Electrochem.*, 2023, **53**, 1389–1403.
60 J. M. Xu, S. H. Chou, Y. Zhang, M. Kumar and S. Y. Shen, *Catalysts*, 2021, **11**(11), DOI: 10.3390/catal11111368.
61 M. P. Hyppólito, J. A. L. Perini, B. F. da Silva, S. M. A. Jorge and M. V. B. Zanoni, *Environ. Sci. Pollut. Res.*, 2022, **29**, 64112–64123.